

## Offshore Transport of Dense Water from the East Greenland Shelf

B. E. HARDEN

*University of East Anglia, Norwich, United Kingdom*

R. S. PICKART

*Woods Hole Oceanographic Institution, Woods Hole, Massachusetts*

I. A. RENFREW

*University of East Anglia, Norwich, United Kingdom*

(Manuscript received 7 November 2012, in final form 4 July 2013)

### ABSTRACT

Data from a mooring deployed at the edge of the East Greenland shelf south of Denmark Strait from September 2007 to October 2008 are analyzed to investigate the processes by which dense water is transferred off the shelf. It is found that water denser than  $27.7 \text{ kg m}^{-3}$ —as dense as water previously attributed to the adjacent East Greenland Spill Jet—resides near the bottom of the shelf for most of the year with no discernible seasonality. The mean velocity in the central part of the water column is directed along the isobaths, while the deep flow is bottom intensified and veers offshore. Two mechanisms for driving dense spilling events are investigated, one due to offshore forcing and the other associated with wind forcing. Denmark Strait cyclones propagating southward along the continental slope are shown to drive off-shelf flow at their leading edges and are responsible for much of the triggering of individual spilling events. Northerly barrier winds also force spilling. Local winds generate an Ekman downwelling cell. Nonlocal winds also excite spilling, which is hypothesized to be the result of southward-propagating coastally trapped waves, although definitive confirmation is still required. The combined effect of the eddies and barrier winds results in the strongest spilling events, while in the absence of winds a train of eddies causes enhanced spilling.

### 1. Introduction

The Denmark Strait is a vital region for the Atlantic meridional overturning circulation in that it provides a major pathway for the return flow of dense water out of the Nordic seas (Dickson and Brown 1994). This is primarily accomplished by the Denmark Strait overflow (DSO), which transports the dense water from a sill depth of 650 m into the deep ocean (Macranders et al. 2005). The DSO is a primary source of the waters that subsequently form the deep western boundary current, the major equatorward pathway of dense water in the Atlantic Ocean.

Recently, an additional pathway for dense water through the region was discovered through high-resolution

hydrographic and velocity measurements across the Greenland continental shelf break south of Denmark Strait. This has been termed the East Greenland Spill Jet (hereafter the spill jet), a narrow, density-driven current along the upper slope above the DSO (Pickart et al. 2005). The name was derived from the hypothesis that the source of the current was dense water passing through Denmark Strait that remained on the Greenland shelf instead of sinking with the DSO plume. The water is then presumed to cascade off the shelf and form the spill jet, although there is evidence that some of the dense water can descend all the way to the depth of main DSO plume (Falina et al. 2012). Through repeat transects of a section across the shelf break south of the strait, the spill jet was established as a consistent feature with densities at times comparable to the DSO, and a mean equatorward transport of  $5.0 \pm 2.2 \text{ Sv}$  ( $1 \text{ Sv} \equiv 10^6 \text{ m}^3 \text{ s}^{-1}$ ; Brearley et al. 2012). This is equivalent to the transport of the DSO at the same latitude (Dickson and Brown 1994) and therefore represents a significant

---

*Corresponding author address:* Benjamin Harden, Woods Hole Oceanographic Institution, 266 Woods Hole Road, Woods Hole, MA 02543.  
E-mail: bharden@whoi.edu

contribution to the return flow of dense water from northern latitudes.

Insights into the processes governing the existence and formation of the spill jet were provided by Magaldi et al. (2011), who implemented a high-resolution numerical ocean model of the region over a 3-month summer period. Their model showed that the spill jet was indeed formed when dense water was forced off the Greenland shelf. The current was highly variable in time, with an average transport comparable to that measured by Brearley et al. (2012). A number of formation mechanisms for the spill jet were hypothesized by Pickart et al. (2005) and Magaldi et al. (2011). These can be classified as (i) spontaneous (no external forcing) spilling, (ii) spilling induced by cyclones passing by on the continental slope emanating from the DSO, and (iii) wind-driven spilling due to the northeasterly Greenland barrier winds. With regard to (i), Magaldi et al. (2011) showed that some spilling events appeared to have no clear forcing mechanism. This spontaneous spilling was theorized to occur due to the inherent instabilities of the East Greenland/Irminger current system at the shelf edge. It is possible that the potentially unstable configuration of dense water flowing near the edge of the shelf, primed to spill, could result in spontaneous spilling episodes.

In addition to this spontaneous process, Magaldi et al. (2011) also showed that many of the spilling events in their model were directly forced by Denmark Strait cyclones located seaward of the shelf break. These eddies are formed when the DSO first descends from the sill and the middle of the water column undergoes intense stretching. To conserve potential vorticity, large relative vorticity is generated that results in cyclonic eddies (Spall and Price 1998). Based on satellite data, a typical eddy has a diameter of 20–40 km and progresses equatorward at a speed of  $25\text{--}30\text{ cm s}^{-1}$  (Bruce 1995). Magaldi et al. (2011) argued that, as these eddies travel equatorward along the continental slope and brush up against the shelf, their leading edges are capable of advecting dense water off the shelf that then adjusts to form the spill jet.

The third hypothesized mechanism (Pickart et al. 2005) is associated with the northeasterly barrier winds in this region. These winds typically form when stable air from an offshore low pressure system is forced toward the high barrier of Greenland and is accelerated along the coast into an intense jet (Schwerdtfeger 1975; Parish 1983). Winds in excess of  $20\text{ m s}^{-1}$  occur frequently in winter (on average once per week; Harden et al. 2011), making this region one of the windiest in the World Ocean (Sampe and Xie 2007; Moore et al. 2008). The barrier winds are downwelling favorable,

and hence could potentially force bottom (dense) shelf water offshore, contributing to the formation of the spill jet. An indirect test of this hypothesis came from the modeling study of Haine et al. (2009), but they found only a weak correlation between the barrier winds and offshore transport on the shelf with no simple relation to the expected Ekman transport. The spill jet–modeling study of Magaldi et al. (2011) was conducted during a period of weak meteorological forcing, and so has little to say regarding the impact of winds.

Although the previous studies provide various insights into the nature and dynamics of the spill jet, to date there have been no direct observations of dense water being advected off the Greenland shelf in this region. Furthermore, the different spilling mechanisms mentioned above need to be verified observationally, and the source of the dense water remains to be clarified. These unresolved issues constitute the motivation for the present study. Using data from a yearlong mooring deployed on the outer shelf 300 km south of Denmark Strait, we address the following specific questions: Is there a net off-shelf transport of dense water south of Denmark Strait? If so, can any of the above-mentioned forcing mechanisms be identified?

The data from the mooring are used to characterize the hydrography and circulation on the outer shelf. To investigate the atmospheric forcing, a global reanalysis product is used. After describing the basic circulation and water masses, including the seasonal variability, evidence is presented for the two external forcing mechanisms that are thought to induce spilling of dense shelf water. This includes the nature of the atmospheric circulation that leads to off-shelf transport. We then present an analysis of the spilling events themselves to help determine the relative importance of the forcing mechanisms, including the degree to which they act in concert with each other. We demonstrate that an off-shelf flux of dense water occurs frequently in this region—presumably feeding the spill jet—and that both offshore oceanic forcing and atmospheric forcing are important.

## 2. Data and methods

### *a. Oceanographic data*

The oceanographic data for this study come from the shoreward-most mooring (hereafter referred to as EG1) of a larger array of seven moorings that was deployed across the southeast Greenland shelf break and slope between September 2007 and October 2008. EG1 resides approximately 10 km inshore of the shelf break in 248 m of water, roughly 300 km south of Denmark Strait (see Fig. 1). As the present study is concerned with the

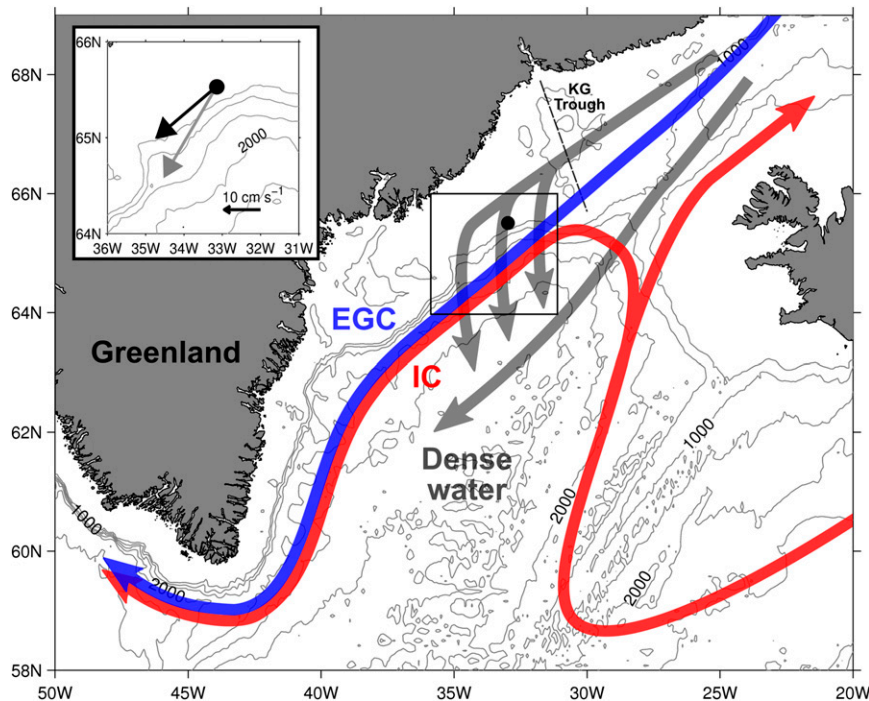


FIG. 1. Schematic of the circulation in the region of interest. Currents shown are the surface-intensified Irminger Current (IC) and East Greenland Current (EGC), and the two pathways of dense water emanating from the Denmark Strait. The mooring location is shown by the black circle. Bathymetric contours are plotted every 500 m. The inset shows an enlarged view of the bathymetry around the mooring site along with the depth-mean current vector (black) and near-bottom velocity (gray) averaged over the yearlong record. The Kangerdlugssuaq Trough is labeled (KG Trough).

offshore transport of dense water from the shelf and not the properties of the adjacent spill jet itself, the data from this shoreward-most mooring alone were used for the investigation. Further analysis of the complete mooring array and a full assessment of the spill jet properties are left to future work. The EG1 mooring contained a combination of hydrographic and velocity profilers in order to obtain vertical traces of the currents and water masses.

### 1) HYDROGRAPHY

A Coastal Moored Profiler (CMP) recorded profiles of temperature and salinity twice daily at 0000 and 0600 UTC from about 10 m above the bottom to the mooring's top float, which was situated approximately 100 m below the sea surface. The data from this device cover the period between the beginning of September, when the mooring was deployed, to the end of April when the CMP motor failed and no further profiles were obtained. The CMP was equipped with a Falmouth Scientific Instruments conductivity–temperature–depth (CTD) recorder. A Sea-Bird Electronics MicroCAT was situated just below the bottom stop of the CMP, which

provided calibration information for the CMP profiles [see Fratantoni et al. (2006) for a description of the methodology]. The CMP data were subsequently interpolated using a Laplacian-spline scheme onto a regular depth-time grid with a temporal and vertical resolution of 6 h and 5 m, respectively. During some periods, the mooring was “blown down” by the strong currents to such an extent that the CMP could not complete full profiles. This resulted in data gaps at some depths for the duration of the blowdown event. These periods were interpolated over if they lasted less than 24 h.

Additional hydrographic measurements were provided by the deep MicroCAT and also by a MicroCAT mounted approximately 40 m above the top float, attached to a buoyant aluminum tube. Unfortunately, this second device only remained above the top float for two months before strong currents likely destroyed the unit's buoyancy and the instrument dropped down below the top float.

### 2) VELOCITY

To measure the velocity of the water column, EG1 contained two upward-facing Teledyne RD Instruments

300-KHz Workhorse Acoustic Doppler Current Profilers (ADCPs), sampling hourly. One was mounted near the base of the mooring and the other on the top float. Consequently, the majority of the water column was covered for the full year. The data from the two ADCPs (which will be referred to as “top” and “bottom”) were concatenated to produce full-depth profiles. We conducted a comparison of the currents measured by the two instruments based on measurements at 110 m for the bottom ADCP and 90 m for the top ADCP. These depths were chosen as a compromise between any systematic difference in the currents over these depths and the paucity of data from the bottom ADCP higher in the water column. The bottom ADCP frequently failed to sample all the way to the top ADCP, but using a depth of 110 m resulted in a 60% data coverage for comparison. The speeds measured by the two instruments agreed very favorably. However, comparison of the ADCP current angles showed a bias between the two instruments that was likely the result of a systematic compass error in one of the two units. After careful consideration, it was deemed that the top ADCP angle measurement was incorrect. The reasoning for this is first that the top ADCP was mounted on the side of a steel top float, which could alter the magnetic field detected by the ADCP’s compass (National Geospatial-Intelligence Agency 2004). Second, the depth-integrated velocity measured by the bottom ADCP is aligned along the local isobaths—as expected for a predominantly geostrophic flow—more closely than the top ADCP.

The correction that we made was to fit a sinusoidal waveform to the difference in the angles between the two ADCPs as a function of the top ADCP angle. This way, for any measured top ADCP angle, there will be a corresponding rotation offset applied to that record. After this rotational correction was implemented, the tidal signal in both records was removed by subtracting out the first five tidal constituents at each depth. The largest of these, the  $K_1$  tide, had an amplitude of approximately  $5 \text{ cm s}^{-1}$ . Subsequent to this, each vertical profile was low-pass filtered vertically using a Butterworth filter with a width of 40 m to remove high-wavenumber fluctuations. Finally, the velocity data were interpolated onto a regular time–depth grid with resolutions of 1 h and 8 m, which filled infrequent short data gaps.

#### *b. Atmospheric reanalysis*

The data used to quantify the timing and location of the atmospheric forcing in the region came from the European Centre for Medium-Range Weather Forecasts (ECMWF) Interim Re-Analysis (ERA-Interim) product, a global atmospheric reanalysis (Berrisford et al. 2009). These data are derived from a spectral model with 60

levels in the vertical, an approximate horizontal resolution of 80 km, and a temporal resolution of 6 h. This product has been previously shown to adequately represent the scale and strength of winds in the region of interest (Harden et al. 2011).

### **3. Oceanographic overview**

#### *a. Hydrography*

South of Denmark Strait the retroflected branch of the Irminger Current joins the East Greenland Current to form a sharp hydrographic front separating the cold, fresh, polar-origin water on the shelf from the warm, salty, subtropical-origin water offshore (Fig. 1). In the mean, the surface-intensified EGC–IC current and its associated front reside just seaward of the shelf break, about 20 km offshore of mooring EG1 (von Appen 2013). However, the front meanders in time, and Irminger water is often present at the mooring site. The temperature and salinity of the upper water column at EG1 show apparent seasonality for the period of the CMP’s operation (see Fig. 2, a 30-day low-pass-filtered representation of these data). In October and early December there are two periods of generally warmer and saltier conditions followed by a general transition to colder, fresher water from January onward. The potential density of the upper layer is dominated by the temperature (Fig. 2) and, as a result, the initially well-stratified waters become denser and destratify through the winter months. The destratification of the upper water column is clearly seen in the buoyancy frequency (Fig. 2d) as a region of low values penetrating deeper into the water column through the winter. This is consistent with the effects of either local or upstream wintertime convection and suggests that this is a seasonal response in the water column.

In the lower water column, the variability over the year is less pronounced. The potential density near the bottom of the shelf (again, dictated primarily by the temperature) is on average greater than  $27.7 \text{ kg m}^{-3}$  and remains reasonably constant over the course of the year (Fig. 2c). The densification and destratification of the upper water column does not reach the bottom of the shelf, at least for the time period up to May. This is seen most clearly in the buoyancy frequency signal: the low values penetrating from the surface, starting in December, do not reach the bottom of the water column.

The contrast between the upper and lower water column is also evident in the data from the MicroCATs (Fig. 3), which operated for the full length of the mooring deployment. The potential density at the bottom of the shelf shows month-to-month variability about

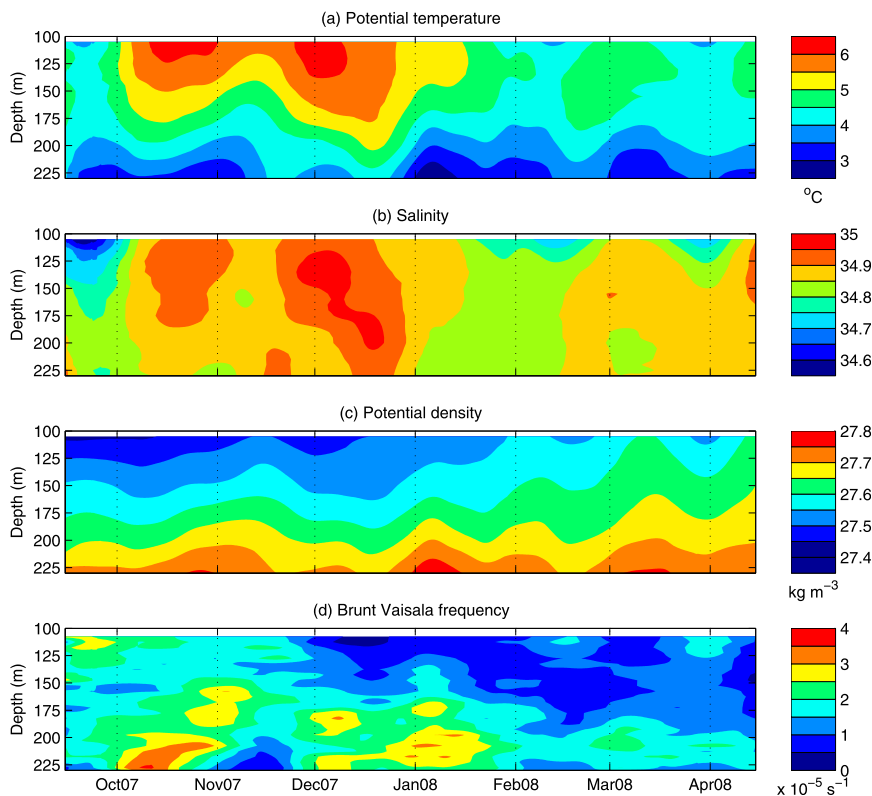


FIG. 2. Hydrographic variables low-pass filtered using a 30-day running-mean filter: (a) potential temperature, (b) salinity, (c) potential density, and (d) Brunt-Väisälä frequency.

a reasonably constant value, even after May when the CMP failed. The mean density at this depth is greater than  $27.7 \text{ kg m}^{-3}$ , as dense as waters previously observed within the spill jet located off the shelf (Brearley et al. 2012). In contrast, higher in the water column, there is an apparent seasonal signal in the MicroCAT record as the water becomes denser during the winter and spring before reversing this trend starting in May. This suggests that, at the time that the CMP failed in late April, the water column had reached its minimum stratification and maximum upper-layer density and was about to restratify.

### b. Velocity

The yearlong-mean flow along the outer shelf is both surface and bottom intensified (Fig. 4). Shallower than about 170 m, the flow is approximately along-isobath (which is directed  $240^\circ$  from north at the location of the mooring; see Fig. 1), but, as the bottom is approached, the current increases in magnitude to over  $25 \text{ cm s}^{-1}$  and veers offshore by  $20^\circ$  (Fig. 4). This can be seen diagrammatically as well in the inset from Fig. 1. The flow at the bottom of the water column has a significant cross-isobath component, demonstrating that there is

a mean off-shelf transport of waters near the base of the mooring.

It is useful for our analysis to decompose the flow into along- and cross-stream components. After some consideration, we used an angle of  $240^\circ$  from north for the along-stream direction. The reason for this was three-fold: As noted above, it corresponds to the direction of the mean flow over the middle and upper portion of the water column; it is the direction of the principal axis of the variance ellipse for the depth-averaged flow; and it is also the approximate orientation of the shelf edge. This latter point allows for the link to be made between cross-stream flow and off-shelf flow. The along-stream flow is positive when directed to the southwest and the cross-stream flow is positive when directed onshore.

Once this coordinate transformation was implemented, coupled empirical orthogonal functions (EOFs) were calculated for the two velocity components in order to characterize the variability of the flow past the mooring (Fig. 5). The first mode, accounting for 59% of the total variance, is barotropic in the along-stream direction and depth dependent in the cross-stream direction with the strongest cross-stream flow at the

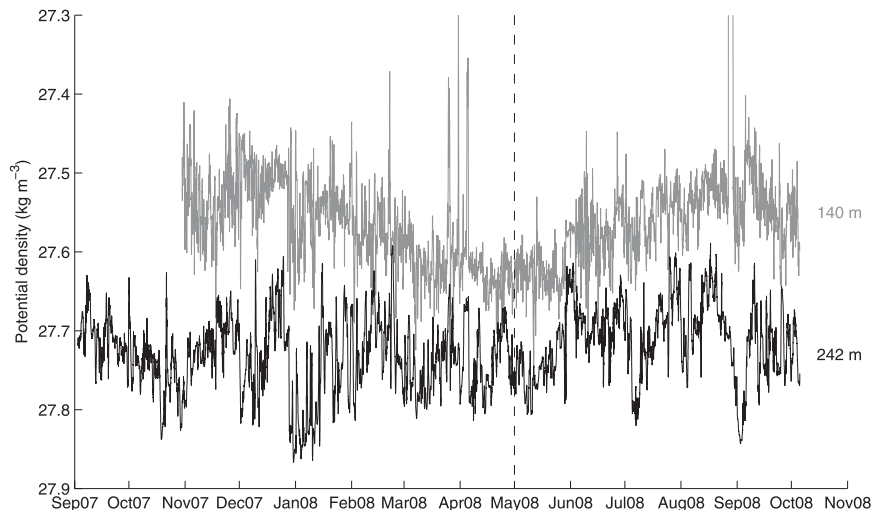


FIG. 3. Potential density measured by the top (gray) and bottom (black) MicroCATs averaged into 6-hourly bins. The depths of the two time series are 140 and 242 m, respectively. Note that the density axis is reversed; larger densities are at the bottom. The upper MicroCAT, initially 40 m above the top float, was knocked down below the top float at the end of October, which is why the upper MicroCAT data shown begin at that time. The dashed line marks the time when the CMP failed.

bottom. The associated time series is almost always positive indicating that the along-stream barotropic mode fluctuates about a defined positive along-stream mean; that is, the direction of the flow is rarely reversed. The associated cross-stream flow has a mean offshore component near the bottom (as has been previously shown), with variability in its magnitude coupled to the strength of the barotropic along-stream flow. Much of the signal captured by this first mode is thought to be related to wind forcing, which is examined in more detail below.

The second coupled EOF mode accounts for an additional 24% of the total variance and is relatively barotropic in the cross-stream velocity with almost no signature in the along-stream flow (Fig. 5). The time series for this mode is centered on zero, indicating that it represents a balanced on–offshore oscillation in the cross-stream velocity. As will be shown later, it is likely that this cross-stream mode is due to the influence of Denmark Strait cyclones that propagate along the continental slope south of Denmark Strait and impinge on the shelf.

### c. Evidence of spilling

We have seen that water as dense as that previously observed in the spill jet, and on occasion exceeding the threshold of DSO water ( $27.8 \text{ kg m}^{-3}$ ), resides near the base of the shelf (Fig. 3). In the mean, this water is directed offshore (Fig. 4). Because the mooring is situated

only 10 km from the shelf break, it is probable that water moving offshore at this site likely crosses the shelf edge. This provides the first observational evidence for the cascading of dense water off the shelf. The eventual fate of this water will depend on the specific density of the water spilled and the amount of entrainment that occurs as the flow descends the slope. As only a small fraction (8%) of the water measured by the bottom MicroCAT is denser than  $27.8 \text{ kg m}^{-3}$  (the threshold for DSO water), it is unlikely that the waters spilled here regularly descend all the way to join the DSO plume [as hypothesized by Falina et al. (2012)]. Formation of the spill jet is more likely at this location, although this does not discount deeper penetration of water spilled upstream of our mooring, nearer Denmark Strait. Regardless of the fate of the water, the offshore transport of dense water from the shelf motivates us to examine the mooring data further in order to understand the forcing mechanisms for the spilling.

## 4. Mechanisms for spilling

As discussed above, three potential mechanisms for the offshore transport of dense water from the shelf are spontaneous spilling, Denmark Strait cyclones, and barrier winds. Here, we consider just the latter two processes; spontaneous spilling is probably occurring at times too but its stochastic nature would make it difficult to discern.

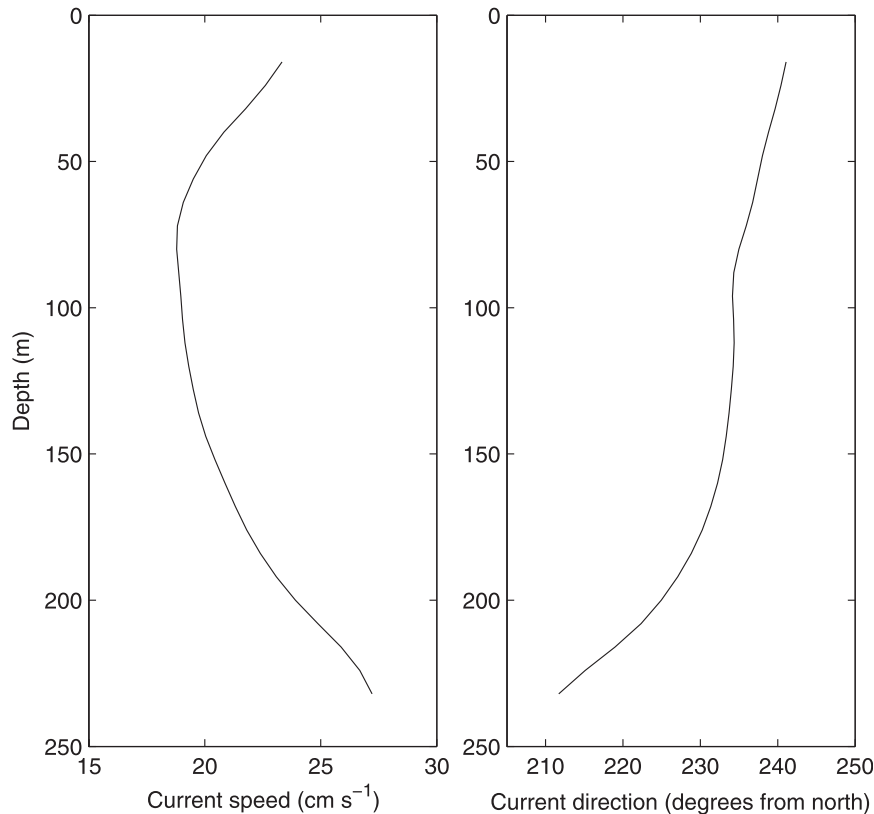


FIG. 4. Mean current speed and direction over the 13-month mooring deployment.

#### *a. Denmark Strait cyclones*

As was shown in the modeling study of Magaldi et al. (2011), the passage of Denmark Strait eddies southward along the continental slope seems to provide the required offshore advection at their leading edges to trigger the spilling of dense water from the outer shelf. Initial evidence for the influence of these eddies comes from the cross correlation of the depth-averaged along- and cross-stream velocities (Fig. 6). Significant correlation between the two velocity components occurs at lags of approximately  $\pm 12$  h. The negative correlation at  $-12$  h corresponds to an offshore-directed current pulse (negative) preceding an along-stream current anomaly (positive), whereas the positive correlation at  $+12$  h is associated with an enhanced onshore current (positive) following the along-stream anomaly. In other words, the correlation pattern indicates a sequence of offshore flow followed by alongshore flow followed by onshore flow, consistent with the expected signature for a mooring located on the shoreward side of a passing cyclonic Denmark Strait eddy. The time between the peaks in the correlation is approximately 24 h, indicating that an eddy

takes on the order of a day or two to pass the mooring site. This is consistent with previous estimates of the propagation speed and diameter of Denmark Strait cyclones (Bruce 1995).

It should be noted that a mooring on the shoreward side of an anticyclonic eddy would produce the same correlation pattern seen in Fig. 6, as the signs of all the velocity components would be reversed. However, detailed inspection of the timing and patterns of the rotational flow at the mooring (Harden 2012) suggests that the features are cyclonic. The signature of eddies is readily apparent throughout the year and manifests itself most clearly in the depth-mean cross-stream velocity record; the energy in this signal was seasonally independent and concentrated between 1 and 4 days (as seen through a wavelet analysis; not shown). This time scale is consistent with that found in the cross-correlation pattern (Fig. 6), but is likely to include the time scale between subsequent eddies as well. The strong eddy signal in the depth-averaged cross-stream flow suggests that the second EOF mode (Fig. 5), a barotropic cross-stream oscillation, is largely representative of eddies and shows that the eddies constitute about 25% of the variance in the velocity record. This is likely to be

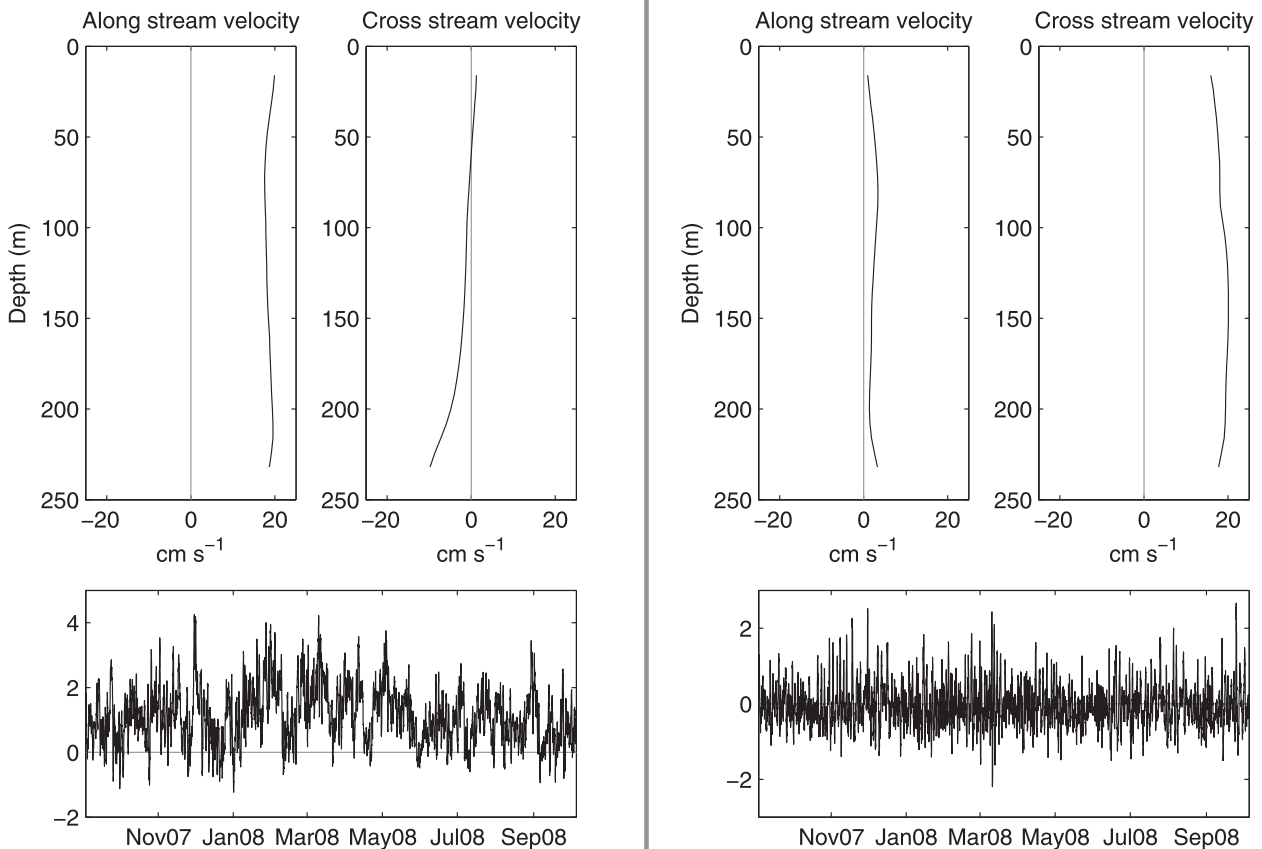


FIG. 5. (left) First and (right) second modes of the coupled EOFs for the along- and cross-stream velocities (positive southward and offshore, respectively). (top) The vertical structure of the mode. (bottom) The associated time series of the mode. The first and second modes account for 59% and 24% of the total variance, respectively.

a lower bound as the eddies' barotropic along-stream signature is probably contributing to the first EOF mode as well. The large cross-stream barotropic velocities associated with a passing eddy provide a suitable offshore advection for the transport of dense water off the shelf and into the spill jet. The importance of eddies for the spilling process will be examined further in section 5.

### b. Barrier winds

It was hypothesized by Pickart et al. (2005) that the downwelling-favorable sense of the barrier winds in this region could be a forcing mechanism for the offshore transport of dense shelf water into the spill jet. The winds should drive Ekman transport onshore in the surface layer, resulting in downwelling and a compensating offshore flow at depth. Because of the convergence in the surface layer at the coast, a cross-shelf sea surface height (SSH) gradient is produced that

results in an along-stream geostrophic current (Allen 1980).

In addition to these local impacts, the winds are also likely to excite coastally trapped waves that will propagate downcoast with the shore to their right (Allen 1980; Mysak 1980; Brink 1991). Their structure and propagation speeds are modified by both topography and stratification, but primary modes are generally associated with a barotropic along-stream velocity signature and travel at speeds on the order of a few hundred kilometers per day (Brink 1982; Pickart et al. 2011). These waves could therefore lead to velocity signals at locations downstream of the direct wind forcing.

The local impacts described above to some extent depend on the scale of the wind forcing. The downwelling cell response will have a similar cross-shelf width to that of the wind forcing. This means that the barrier winds that force this kind of response at the mooring site need to be at least the width of the shelf, which at the mooring location is on the order of 100 km. The



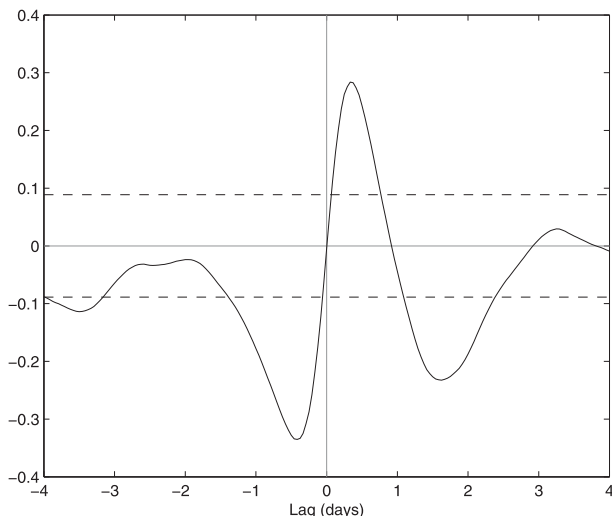


FIG. 6. Cross correlation of the depth-mean along- and cross-stream velocity. Correlations at positive (negative) lags indicate that the along-stream velocity leads (trails) the cross-stream velocity. The 95% confidence interval is shown with dashed lines.

upstream length scale of the wind forcing is also important. At the back end of the region of wind forcing, the signal associated with the absence of wind will propagate downcoast into this region. This will have the effect of eroding the SSH anomaly where the winds are acting and will disrupt the idealized two-dimensional downwelling cell within this region, most likely resulting in a reduction of the offshore flow below the surface layer (Allen 1976). This latter fact could be important if we are trying to observe offshore transport at depth associated with barrier winds.

It should be noted that large parts of the Greenland shelf are partially ice covered for a significant portion of the year. This will have the effect of modifying the momentum input to the ocean from the winds and hence impact the forcing mechanisms outlined above. Depending on the type of ice cover, the impacts will be different. Landfast and 100% ice cover will clearly limit the momentum input, but there is evidence that partial ice cover enhances the surface stress imparted to the ocean (Williams et al. 2006; Schulze and Pickart 2012; Pickart et al. 2013). For the year of our investigation, the ice was patchy and mobile over much of the shelf (and the mooring) during the winter months, as seen from Advanced Microwave Scanning Radiometer for Earth Observing System (AMSR-E) sea ice concentration data (not shown). This information, along with the robustness of the following results, suggests that the sea ice is not significantly impacting the ability of the wind to impart stress to the shelf waters.

The velocity data from the mooring, in conjunction with the high-resolution meteorological reanalysis, allow

us to investigate the wind-forced processes and assess to what degree they could force the spilling of dense water. To quantify the times and strengths of barrier winds over the yearlong mooring deployment, the meteorological data from ERA-Interim were subject to a barrier wind detection routine similar to that used in Harden et al. (2011). Specifically, we computed the along-coast ( $240^\circ$  from north) component of the 10-m velocity time series at the nearest ERA-Interim grid point to the mooring site. Barrier wind events were defined as maxima in this time series greater than  $15 \text{ m s}^{-1}$  and separated in time by at least 24 h.

The results of this detection routine are shown in Fig. 7. In total, 49 events were detected, equivalent to one per week. It is clear, however, that many of the strongest events occur in the winter months; there are many more events between September and May than there are in the summer months. Times when the wind is weak and directed up the coast (in the opposite direction of barrier winds) are also apparent. It can be seen that, for the year that the mooring was deployed, the barrier winds are strong and frequent, suggesting a high chance of detecting a response in the ocean.

The composite image of the 10-m wind field and mean sea level pressure for the 49 detected barrier winds (Fig. 7) shows a picture typical of barrier winds in the region (e.g., Moore and Renfrew 2005; Harden et al. 2011). A composite low pressure system is located in the central Irminger Sea with a depth of 986 hPa. This low directs air toward the southeast coast of Greenland into a composite barrier wind at its maximum over the mooring site. The composite barrier wind is wide enough to cover the entire shelf (as it is for most of the individual composite members; not shown), meeting the width criteria for a downwelling response to be present at the mooring, as posited above. Evidence for some of the expected ocean impacts is now presented.

It is hard to find specific examples of a local wind that produces the expected downwelling response at the mooring. The reason for this is because, as previously shown, the velocity record at the mooring site is dominated by rotational signals from eddies throughout the year. However, the downwelling cell can be readily identified in a lagged composite of the cross-stream velocity anomaly at the times of the 49 local barrier wind events (Fig. 8). There is enhanced onshore flow of nearly  $10 \text{ cm s}^{-1}$  in the upper layer and a return flow, at a slight lag, near the bottom with a magnitude of  $6 \text{ cm s}^{-1}$ . Thus, it appears that, although individual cases are difficult to discern, the composite effect of all barrier winds (once the random eddies have been

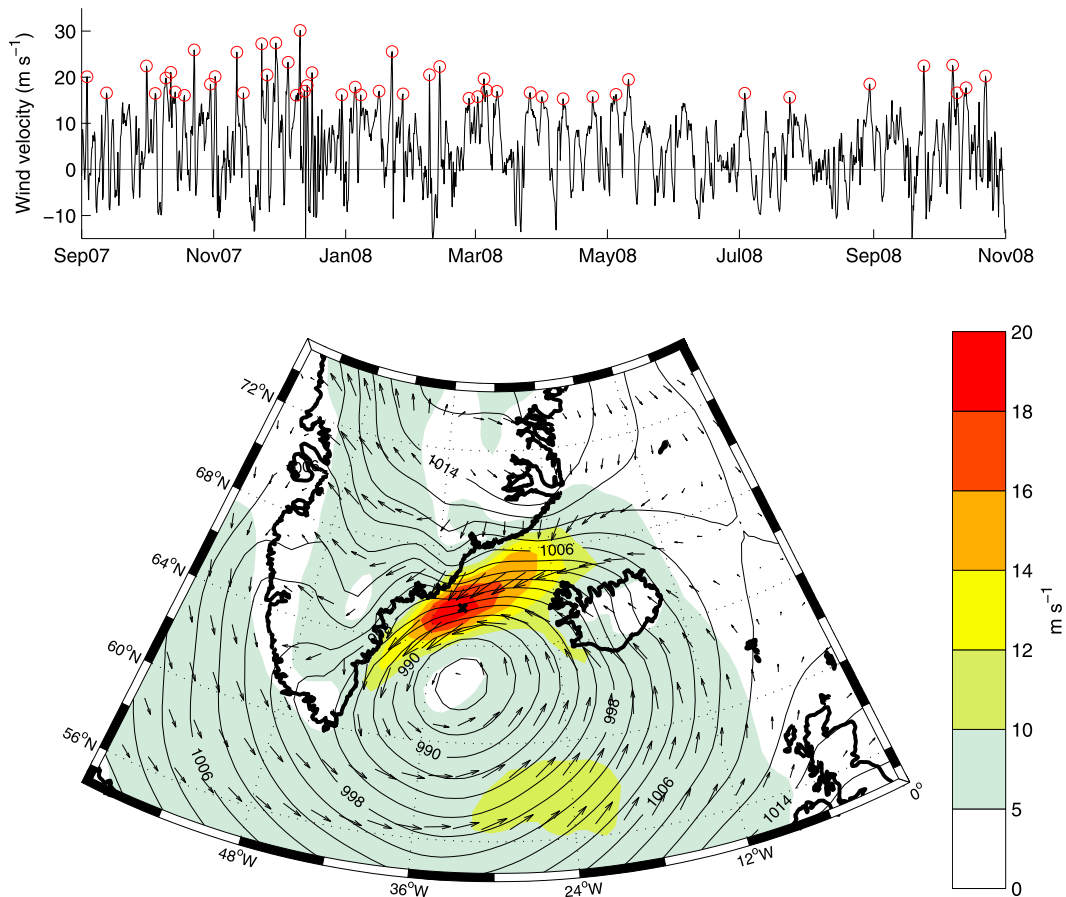


FIG. 7. (top) Along-coast 10-m wind velocity from the nearest ERA-Interim grid point to the EG1 mooring. Detected barrier wind events are depicted by the red circles. (bottom) Composite of the 10-m wind speed (color) from the 49 detected barrier wind events. The composite mean sea level pressure (contours) is shown every 2 hPa and the composite wind vectors are plotted at every third grid point. The EG1 mooring location is indicated by the black cross.

averaged out) is the expected downwelling cell that will advect dense bottom water offshore.

In addition to the cross-stream composite signal, there is also a surface-intensified along-stream velocity anomaly extending throughout the water column (Fig. 8). This can be understood as the along-stream response to the SSH anomaly set up by the onshore surface transport as described above. Both the along-stream acceleration and the offshore return flow are enhanced if the 49 events are subsampled based on which ones are concurrent with a strong wind extending approximately 500 km upstream (not shown). This is tantamount to only compositing the long barrier wind events and, as described previously, should be representative of events that produce the strongest, most persistent downwelling. That the composite ocean signal is strengthened when only the long barrier winds are used provides us with confidence that the signal observed is indeed that of downwelling.

The location of wind action that excites the strongest along-stream response is not, however, at the mooring site. The left-hand panel of Fig. 9 shows the maximum in the lagged correlation of the along-coast winds at every point in the domain with the depth-mean along-stream current at the mooring site. The correlation is clearly strongest not at the mooring site, but in a region extending upstream into the central Denmark Strait.

An analysis correlating the winds with the bottom cross-stream velocity at the mooring site yields a similar pattern, albeit with a reversal of sign (i.e., increased offshore flow; Fig. 9, right). Again, the largest correlations occur in a region extending upstream from the mooring. If the ocean response to winds were just a local downwelling signal, it might be expected that the maximum correlations would be found nearer to the mooring site. Indeed, when a similar analysis is conducted between the along-coast wind and cross-stream ocean velocity at the surface, the strongest correlations are

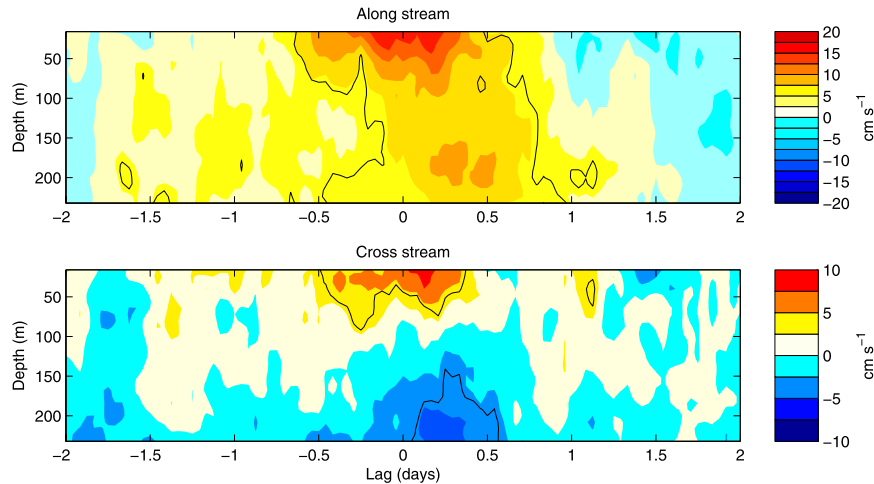


FIG. 8. Lagged composites of (top) along- and (bottom) cross-stream velocity anomalies, relative to the yearlong mean, centered on the times of detected barrier winds shown in Fig. 7. All 49 events comprised the composite. The black contour indicates the regions that are statistically significant at the 95% confidence level.

found at the mooring site, indicative of local forcing (not shown).

The pattern seen in the correlation maps of Fig. 9 can be represented explicitly in the mooring data through ocean composites for the times of 59 barrier winds detected in the correlation maxima upstream of the mooring site (Fig. 10). These upstream barrier wind events were detected in the same manner as those detected locally. At a lag of half a day after the wind intensifies in the Denmark Strait, a large nearly barotropic along-stream current anomaly appears at the mooring site. This is coupled to a bottom-intensified offshore flow of larger magnitude than the local response seen in Fig. 8.

We believe that the mechanism responsible for the signal seen in the composite image of Fig. 10 is different than that for local forcing. We hypothesize that the

downcoast propagation of coastally trapped waves is responsible, an idea that is motivated for the following reasons. First, the location of barrier wind action is upstream of the mooring and would require downcoast propagation in the ocean to excite any response at the mooring site. Second, the time lag between forcing and the composite response is consistent with the propagation speed of a first-mode coastally trapped wave—on the order of  $800 \text{ km day}^{-1}$  for the East Greenland shelf (Brink 1982). Finally, the lack of significant onshore flow in the composite indicates that the signal is not indicative of a simple Ekman downwelling cell.

We surmise then that, in addition to locally forced downwelling, nonlocal winds are capable of exciting coastally trapped waves, which, through their downcoast propagation, induce a strong barotropic along-stream

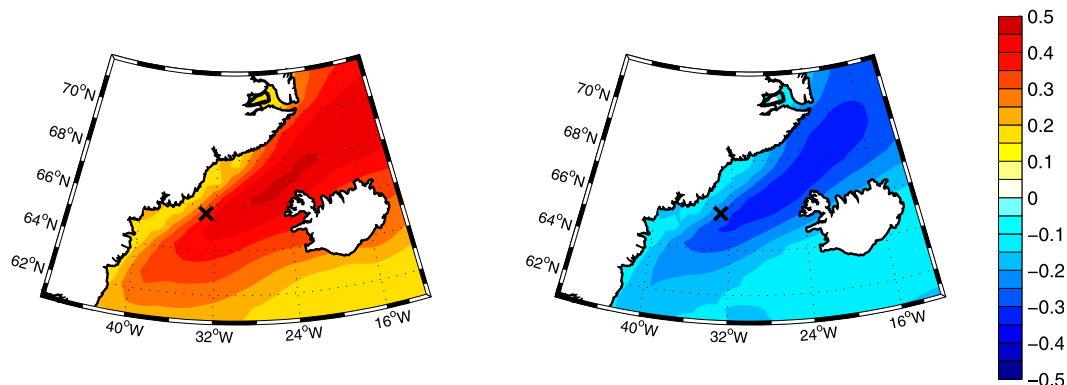


FIG. 9. Max of the lagged correlations of the along-coast wind velocity at all points in the domain with the (left) depth-mean along-stream velocity and (right) bottom cross-stream velocity. Correlation max are significant at 95% confidence. The black cross indicates the location of the EG1 mooring.

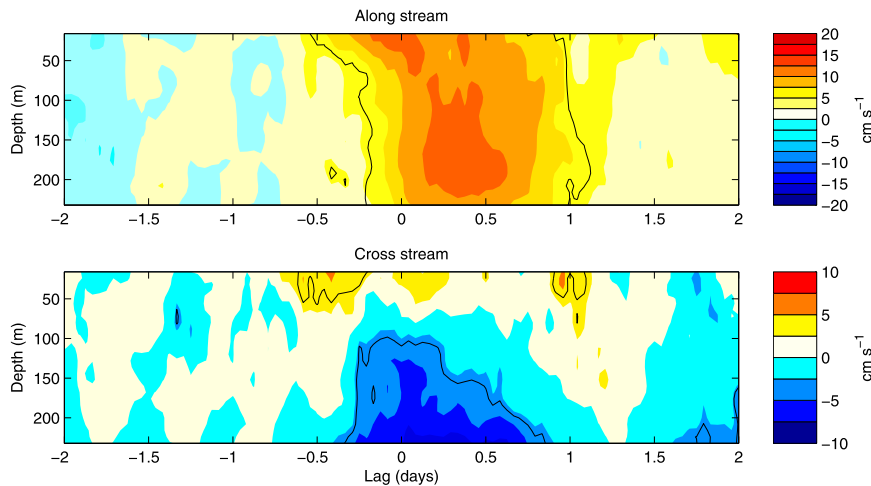


FIG. 10. As in Fig. 8, but for the 59 barrier winds detected at an upstream location ( $67.7^{\circ}\text{N}$ ,  $25.3^{\circ}\text{W}$ ). This location is just shoreward of the max in the along-stream correlation map shown in the left panel of Fig. 9.

response at the shelf edge that is coupled to an offshore flow near the bottom. This generation of spilling in conjunction with an along-stream velocity anomaly is reminiscent of the first EOF mode (Fig. 5). That is, every time a barotropic along-stream acceleration is observed it is coupled to a bottom-trapped cross-stream flow.

The relative paucity of data from the mooring during these events makes it difficult to confirm the role of coastally trapped waves or the ways in which any along-stream anomalies in these waves might be coupled to the offshore accelerations observed. Furthermore, although we have made a distinction between locally forced downwelling and the upstream excitation of coastally trapped waves, these mechanisms are part of a consistent shelf-wide response to wind forcing and so cannot be treated as entirely independent processes. As such, to definitively test our hypothesis requires significant further study, including the use of modeling, and hence is beyond the scope of the present analysis. However, in section 6 we discuss possible mechanisms for the coupling of along-stream anomalies to spilling.

## 5. Observed spilling

We now consider the spilling process itself and analyze this within the context of the two driving mechanisms presented above. The potential for the mooring velocity data to capture the signature of spilling events was shown earlier in section 3. As such, we use the cross-stream velocity from the bottommost bin of the ADCP record as a proxy for the magnitude of spilling (Fig. 11). This time series indicates that the spilling is intermittent,

with variability on a range of scales from hours to months.

### a. High-frequency variability

To examine individual spilling events, a detection method (similar to that used for the barrier winds) was employed. The criteria for an event are that the magnitude of the bottom cross-stream velocity must be larger than  $30 \text{ cm s}^{-1}$  (qualitatively similar results are found for other thresholds), directed offshore, and separated from another spilling event by at least 24 h. If two events were detected less than 24 h apart, the larger of the two events was chosen. This detection method returned 94 events, equivalent to about two spilling events per week for the yearlong record. These events are marked in Fig. 11. An additional constraint was considered that required the density of the bottom MicroCAT to be greater than  $27.7 \text{ kg m}^{-3}$  (which is the typical density of the spill jet water; Pickart et al. 2005; Brearley et al. 2012). Only a quarter of the 94 events are discarded if this extra criterion is used. However, because there is reasonably dense water at all times on the shelf and it is likely denser than that found directly offshore at this depth (Brearley et al. 2012), this was deemed an unnecessary constraint, especially as the subsequent analysis is unchanged and a larger number of events increases the robustness of the results.

Lagged composites of the along- and cross-stream velocity anomalies, relative to a 5-day running mean calculated at every depth, for the times of all detected spilling events are shown in Fig. 12a. The use of the running mean allows us to isolate the high-frequency signature of the spilling, which we will largely attribute

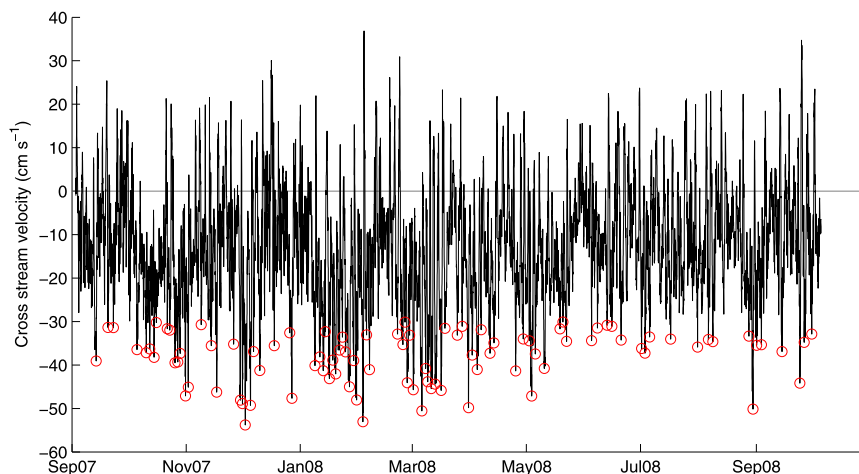


FIG. 11. Cross-stream velocity from the lowest ADCP bin at a depth of 232 m. Detected spilling events are marked with red circles.

to eddies. Five days was chosen for the width of the high-pass filter in order to capture the signal from eddies, both the rotations of individual cyclones and the time between them (qualitatively similar results are obtained for larger filter widths, but this value produces the cleanest response). The resulting composite shows the unmistakable patterns of an eddy. Not surprisingly, the offshore flow associated with the detected spilling feature is the largest signal in the figure because at zero lag this is constrained to be large. On either side of this, both at positive and negative lags, is a sequence of enhanced on- and offshore cross-stream velocities with a time scale of about two days. This period is consistent with that attributed earlier to the passage of eddies (Fig. 6). The along-stream flow has a similar pattern of positive and negative anomalies with a similar period, but shifted a quarter of a period ahead of the cross-stream flow. This pattern describes rotational flow consistent with the passing of a cyclonic eddy offshore of the mooring, the leading edge of which is drawing water offshore and consequently acting as the trigger for spilling. This is in agreement with the eddy-forced spilling mechanism in the numerical model of Magaldi et al. (2011).

To further investigate this pattern under slightly different conditions, the 94 events were subsampled based on whether they occurred coincidentally with strong or weak local winds. The strong wind threshold was  $12.7 \text{ m s}^{-1}$ , which is the upper quartile of the along-coast 10-m wind velocities for the times of spilling, producing 23 events. The low wind criterion was that the magnitude of the along-coast 10-m wind velocity was less than  $5 \text{ m s}^{-1}$ , producing 28 events.

The high wind composite (Fig. 12b) shows that when there is a strong local wind, only a slightly larger offshore

flow occurs at the bottom ( $\sim 1 \text{ cm s}^{-1}$ ) but the degree of depth dependency in the cross-stream signal is greater. The along-stream flow that follows the spilling is also much stronger. Both of these features are consistent with the response associated with wind forcing (Figs. 8 and 10) wherein the winds drive strong along-stream currents and associated bottom-intensified offshore flow. The composite still has the signature of a single eddy, however, suggesting that even under high local wind speed conditions the precise timing of the spilling is still largely dictated by the eddy. The local wind appears to enhance the effect of the eddies and consequently produce some of the strongest spilling events.

When there are weak local winds (Fig. 12c), what becomes apparent is a long chain of eddies extending backward in time from zero lag, but not extending into positive lags. This implies that, in the absence of local wind forcing, a single eddy by itself is not strong enough to produce the largest spilling events. Rather, the progressive influence of a chain of closely packed eddies is necessary in order for the spilling to be strong enough. Presently it is unclear what causes the enhanced spilling due to a close train of eddies, but some insight is provided from Fig. 8 of Spall and Price (1998). Their idealized simulations of Denmark Strait eddies show a complex flow field associated with a train of eddies, but there is evidence of an increased offshore transport at the leading edge of an eddy that follows closely behind another.

It should perhaps be noted that, although the precise timing of spilling events has been largely attributed to eddies, there are likely to be other processes at work that will lead to spilling, such as internal instabilities and individual strong wind events. These mechanisms may be masked in the spilling composites by the strong

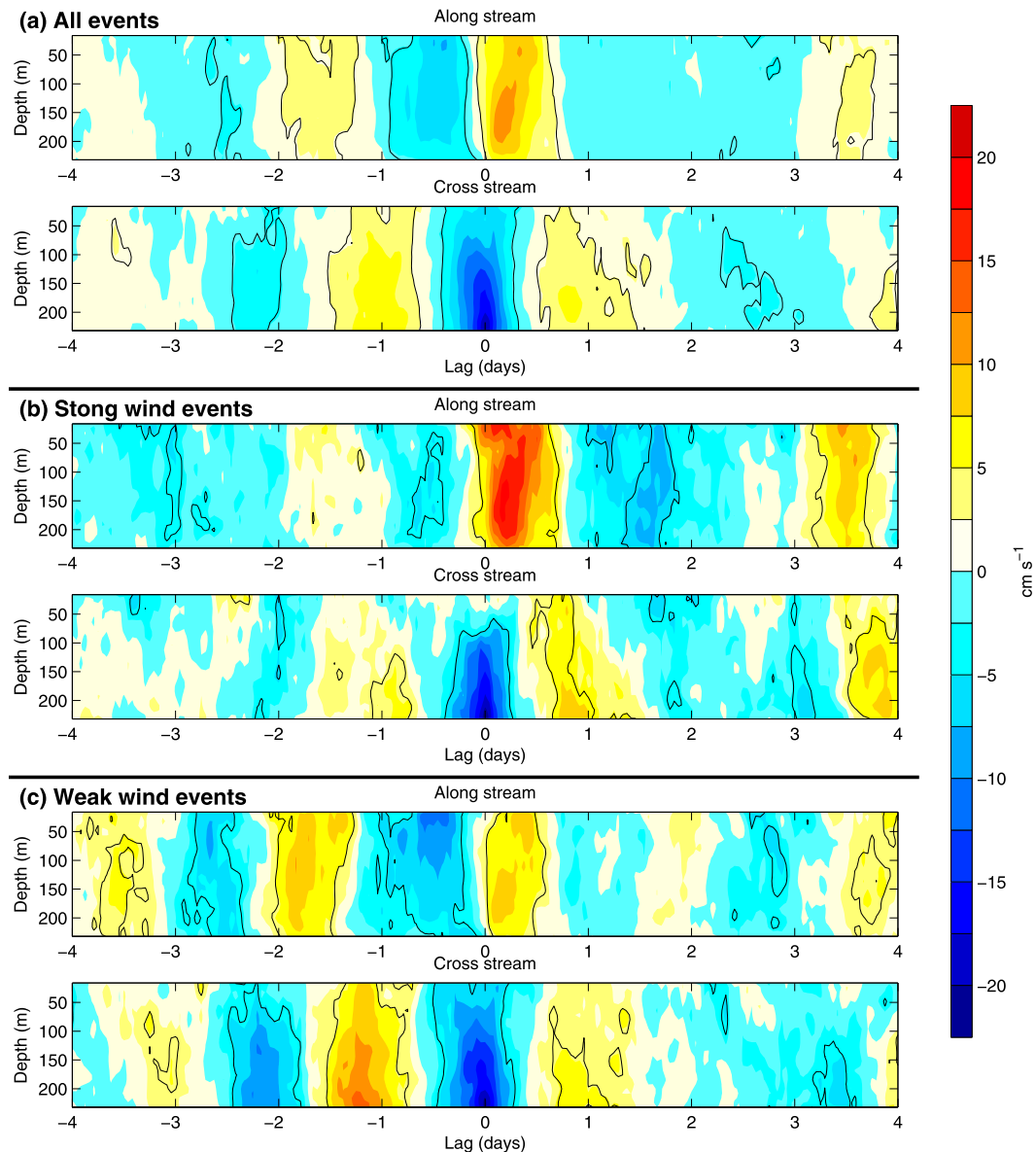


FIG. 12. (a) Lagged composites of 5-day high-pass-filtered along- (top) and cross-stream (bottom) currents from the times of the 94 spilling events shown in Fig. 11. The black contours indicate anomalies that are statistically significant at 95% confidence. (b) As in (a), but for the 23 events concurrent with a local along-coast wind velocity greater than  $12.7 \text{ m s}^{-1}$  (upper quartile of wind velocities for all 94 spilling events). (c) As in (a), but for the 28 events that are concurrent with a local along-coast wind velocity magnitude less than  $5 \text{ m s}^{-1}$ .

coherence of the eddy structures or they may be producing spilling in the region between the mooring and the shelf edge, meaning they are missed from the EG1 observational record.

#### *b. Low-frequency variability*

It has been demonstrated above that eddies are responsible for much of the higher-frequency variability in the strongest spilling events, but there is variability as

well in spilling at scales longer than a couple of days. In particular, there are sustained periods of cross-stream flow larger than the mean, for example in January and early March, and also periods of reduced cross-stream flow, for example in mid-February and early June (Fig. 11). It should be noted that all of the strongest spilling events detected cluster at times of larger mean cross-stream flow. This lower-frequency variability is illustrated more clearly in Fig. 13, which shows the



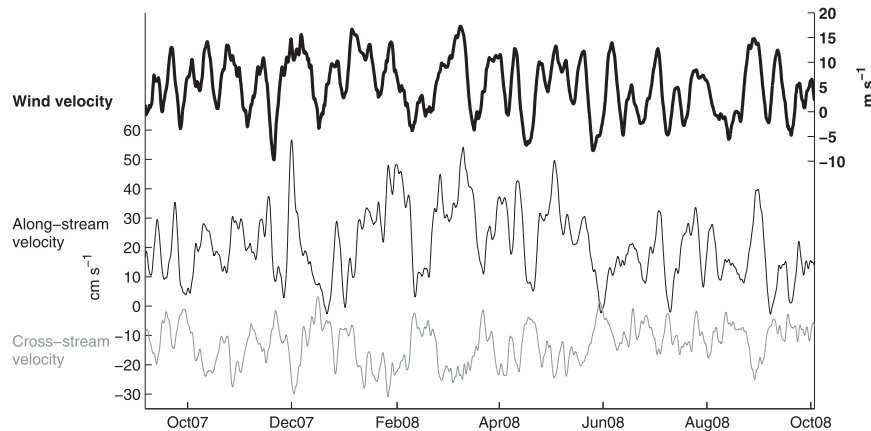


FIG. 13. Five-day low-pass-filtered along-coast wind velocity (bold black) from a location upstream of the mooring site ( $67.7^{\circ}\text{N}$ ,  $25.3^{\circ}\text{W}$ ). The low-pass-filtered depth-mean along-stream velocity from the mooring is the black curve, and the low-pass-filtered cross-stream velocity from the bottom-most ADCP bin at 232 m is the gray curve. The axis on the left applies for both the along- and cross-stream velocities.

5-day low-pass-filtered 10-m wind velocity from the upstream location used previously (for Fig. 10) and the low-pass-filtered depth-mean along-stream and bottom cross-stream velocities from the mooring.

The coupling of the depth-mean along-stream velocity with the bottom cross-stream velocity (previously shown as the first EOF mode; Fig. 5) shows up clearly when these velocity records are subjected to the low-pass filter: there is a strong anticorrelation ( $r = -0.68$ , significant at 99% confidence) between these variables (bottom two time series of Fig. 13). The impact of the upstream wind on these currents is also clear when filtered in the same manner (Fig. 13). In particular, periods of stronger or more frequent strong winds produce an increase in the along-stream velocity and a larger offshore-directed flow at the bottom. The wind time series is significantly correlated with both the along- and cross-stream time series. The lagged correlation between the wind and the two velocity time series has a maximum of 0.58 (significant at 99% confidence) at a lag of 2 days (the wind leads the ocean response).

The actual time scale for individual wind events is almost always smaller than the threshold used for the low-pass filter (5 days), so individual storms are not being resolved in this time series. Therefore, what is shown is the average windiness of a period of time (i.e., either numerous or extended wind events). The time scale of the impact of the wind on the ocean is likely to be contained within the higher-frequency analysis, but the eddy signatures are so strong that it cannot be easily isolated. It is only by considering the lower-frequency variability (over which time period the balanced flow pattern of the eddies is averaged out) that the full

significance of the wind's impact on spilling is readily apparent.

## 6. Conclusions and discussion

Data from a yearlong profiling mooring deployed on the outer East Greenland shelf south of Denmark Strait have allowed us to elucidate the processes responsible for the cascading of dense water off the shelf. On average, the water on the bottom of the shelf has a density greater than  $27.7 \text{ kg m}^{-3}$ , which is as dense as the water observed in previous spill jet hydrographic measurements (Pickart et al. 2005; Brearley et al. 2012). While there is considerable variability in the bottom density record, no seasonal signal was apparent. The mean velocity in the central part of the water column is directed along the isobaths, while the flow veers offshore by  $20^{\circ}$  near the bottom with a speed exceeding  $25 \text{ cm s}^{-1}$ . This provides the first observational evidence of off-shelf flow of dense water that likely feeds the East Greenland Spill Jet.

Two potential forcing mechanisms for triggering dense water-spilling events were investigated. The first is due to the passage of Denmark Strait cyclones as seen in the model simulations of Magaldi et al. (2011). The influence of these eddies was readily apparent in the mooring velocity record as a clockwise rotation of varying magnitude. This signal has a characteristic time scale on the order of one day, consistent with previous measurements of Denmark Strait eddy features. The cyclones were shown to be the primary controller of spilling events via offshore advection at their leading edges. The second forcing mechanism considered was

that of downwelling-favorable barrier winds, which occur frequently in this region. Evidence of the impact of these winds was also observed in the velocity record. Local winds produce a downwelling Ekman cell that leads to offshore flow at the bottom of the shelf. There is also evidence that upstream winds can trigger coastally trapped waves that propagate down the coast exciting along-stream accelerations that are coupled to the offshore transport of dense water. The combined effect of eddies and barrier winds result in the strongest spilling events, while, in the absence of winds, a train of eddies causes enhanced spilling.

The result that is least well understood in our study is the coupling of along-stream velocity anomalies, which we have argued are produced by coastally trapped waves, with bottom-intensified offshore flow. While the data presented do not allow us to fully elucidate this coupling, we are able to use the results obtained in this study to discuss possibilities.

One possible explanation for the coupling is that of a bottom Ekman layer. As the along-stream velocity anomaly is set up, bottom friction and the Coriolis force will act to cause a veering to the left (offshore) near the bottom. It is unlikely, however, that this is the cause of the observed offshore flow for two reasons. First, the depth of this Ekman layer would have to be on the order of 100 m, which is large for a typical Ekman layer, and second the current speed in a bottom Ekman spiral weakens toward the bottom, while the magnitude of the measured flow during these events increases toward the bottom. Consequently, we believe that a bottom Ekman layer can be discounted as the cause of the bottom-intensified offshore flow.

It is possible that the wind-forced velocities are interacting in a nonlinear manner with the eddies propagating along the East Greenland slope. In our analysis, we have averaged over many wind events in order to remove the eddy signal. It is implicit within this method that we can linearly sum the impact of eddies and winds in any observed ocean response; by averaging over many wind events we would thus be subtracting the eddy signal and recovering the wind signal alone. However, if the wind response is nonlinearly influencing the flow pattern produced by an individual eddy, we may see some of this interaction in our composite images.

Another explanation could be the impact of the complex and highly variable atmospheric configurations in this region. Barrier winds can be centered at any location along the coast, their spatial and temporal scales are wide ranging, and they can transit up or down the coast or remain stationary. All of these factors likely influence the oceanic response and any coastal waves generated, and are deserving of further study.

Finally, it is likely that there will be interactions of the along-stream velocity anomalies with the complex bathymetry of the shelf. The East Greenland shelf varies significantly in width and depth, and has a number of other complex topographic features (see Fig. 1). Of potential importance are the widening of the shelf through the Denmark Strait, the lip on the outer shelf in the vicinity of the mooring, and the deep Kangerdlugssuaq Trough, which cuts into the shelf upstream of the mooring site with a depth of over 500 m (Fig. 1). This latter feature is likely to be very important in the redistribution of energy in any coastally trapped waves. Obstructions to the propagation of an along-coast wave should result in the scattering of the wave energy into different directions and higher wave modes. Higher-mode coastally trapped waves have been shown to be increasingly bottom trapped (Huthnance 1978), so they are a good candidate for explaining the bottom-intensified offshore flow seen in our composites. This explanation, however, implies that the results obtained in this study might be region specific; that is, the wind-forced mechanisms seen at the mooring may not be representative of mechanisms at play along the wider shelf break, but could instead be produced by a local topographic features.

*Acknowledgments.* The authors wish to thank Paula Fratantoni, Frank Bahr, and Dan Torres for processing the mooring data. The mooring array was capably deployed by the crew of the R/V *Arni Fridriksson* and recovered by the crew of the R/V *Knorr*. We thank Hedinn Valdimarsson for his assistance in the field work. Ken Brink provided valuable insights regarding the dynamics of shelf waves. Funding for the study was provided by National Science Foundation Grant OCE-0722694, the Arctic Research Initiative of the Woods Hole Oceanographic Institution. We also wish to thank the Natural Environment Research Council for Ph.D. studentship funding, and the University of East Anglia's Roberts Fund and Royal Meteorological Society for supporting travel for collaboration.

## REFERENCES

- Allen, J. S., 1976: Some aspects of the forced wave response of stratified coastal regions. *J. Phys. Oceanogr.*, **6**, 113–119.
- , 1980: Models of wind-driven currents on the continental shelf. *Annu. Rev. Fluid Mech.*, **12**, 389–433, doi:10.1146/annurev.fl.12.010180.002133.
- Berrisford, P., D. Dee, M. P. Fielding, K. Fuentes, S. Kobayashi, and S. Uppala, 2009: The ERA-Interim Archive. ECMWF Tech. Rep. 1, 16 pp. [Available online at <http://www.ecmwf.int/publications/library/do/references/show?id=89203>.]
- Brearely, J. A., R. S. Pickart, H. Valdimarsson, S. Jonsson, R. W. Schmitt, and T. W. Haine, 2012: The East Greenland boundary



- current system south of Denmark Strait. *Deep-Sea Res. I*, **63**, 1–19, doi:10.1016/j.dsr.2012.01.001.
- Brink, K. H., 1982: A comparison of long coastal trapped wave theory with observations off Peru. *J. Phys. Oceanogr.*, **12**, 897–913.
- , 1991: Coastal-trapped waves and wind-driven currents over the continental shelf. *Annu. Rev. Fluid Mech.*, **23**, 389–412, doi:10.1146/annurev.fl.23.010191.002133.
- Bruce, J. G., 1995: Eddies southwest of the Denmark Strait. *Deep-Sea Res. I*, **42**, 13–29, doi:10.1016/0967-0637(94)00040-Y.
- Dickson, R. R., and J. Brown, 1994: The production of North Atlantic Deep Water: Sources, rates, and pathways. *J. Geophys. Res.*, **99**, 12 319–12 341.
- Falina, A., A. Sarafanov, H. Mercier, P. Lherminier, A. Sokov, and N. Daniault, 2012: On the cascading of dense shelf waters in the Irminger Sea. *J. Phys. Oceanogr.*, **42**, 2254–2267.
- Fratantoni, P. S., S. Zimmermann, R. S. Pickart, and M. Swartz, 2006: Western Arctic Shelf–Basin Interactions Experiment: Processing of moored profiler data from the Beaufort Shelf Edge mooring array. Woods Hole Oceanographic Institution Tech. Rep. WHOI-2006-15, 29 pp, doi:10.1575/1912/1429.
- Haine, T. W. N., S. Zhang, G. W. K. Moore, and I. A. Renfrew, 2009: On the impact of high-resolution, high-frequency meteorological forcing on Denmark Strait ocean circulation. *Quart. J. Roy. Meteor. Soc.*, **135**, 2067–2085, doi:10.1002/qj.505.
- Harden, B. E., 2012: Barrier winds off southeast Greenland and their impact on the ocean. Ph.D. thesis, University of East Anglia, 172 pp.
- , I. A. Renfrew, and G. N. Petersen, 2011: A climatology of wintertime barrier winds off southeast Greenland. *J. Climate*, **24**, 4701–4717.
- Huthnance, J. M., 1978: On coastal trapped waves: Analysis and numerical calculation by inverse iteration. *J. Phys. Oceanogr.*, **8**, 74–92.
- Macrander, A., U. Send, H. Valdimarsson, S. Jónsson, and R. H. Käse, 2005: Interannual changes in the overflow from the Nordic seas into the Atlantic Ocean through Denmark Strait. *Geophys. Res. Lett.*, **32**, L06606, doi:10.1029/2004GL021463.
- Magaldi, M. G., T. W. N. Haine, and R. S. Pickart, 2011: On the nature and variability of the East Greenland Spill Jet: A case study in summer 2003. *J. Phys. Oceanogr.*, **41**, 2307–2327.
- Moore, G. W. K., and I. A. Renfrew, 2005: Tip Jets and Barrier Winds: A QuikSCAT climatology of high wind speed events around Greenland. *J. Climate*, **18**, 3713–3725.
- , R. S. Pickart, and I. A. Renfrew, 2008: Buoy observations from the windiest location in the world ocean, Cape Farewell, Greenland. *Geophys. Res. Lett.*, **35**, L18802, doi:10.1029/2008GL034845.
- Mysak, L., 1980: Topographically trapped waves. *Annu. Rev. Fluid Mech.*, **12**, 45–76, doi:10.1146/annurev.fl.12.010180.000401.
- National Geospatial-Intelligence Agency, 2004: Handbook of Magnetic Compass Adjustment. National Geospatial-Intelligence Agency, 45 pp.
- Parish, T. R., 1983: The influence of the Antarctic Peninsula on the wind field over the western Weddell Sea. *J. Geophys. Res.*, **88**, 2684–2692.
- Pickart, R. S., D. J. Torres, and P. S. Fratantoni, 2005: The East Greenland Spill Jet. *J. Phys. Oceanogr.*, **35**, 1037–1053.
- , M. A. Spall, G. W. K. Moore, T. J. Weingartner, R. A. Woodgate, K. Aagaard, and K. Shimada, 2011: Upwelling in the Alaskan Beaufort Sea: Atmospheric forcing and local versus non-local response. *Prog. Oceanogr.*, **88**, 78–100, doi:10.1016/j.pocean.2010.11.005.
- , —, and J. T. Mathis, 2013: Dynamics of upwelling in the Alaskan Beaufort Sea and associated shelf–basin fluxes. *Deep-Sea Res. I*, **76**, 35–51.
- Sampe, T., and S.-P. Xie, 2007: Mapping high sea winds from space: A global climatology. *Bull. Amer. Meteor. Soc.*, **88**, 1965–1978.
- Schulze, L. M., and R. S. Pickart, 2012: Seasonal variation of upwelling in the Alaskan Beaufort Sea: Impact of sea ice cover. *J. Geophys. Res.*, **117**, C06022, doi:10.1029/2012JC007985.
- Schwerdtfeger, W., 1975: The effect of the Antarctic Peninsula on the temperature regime of the Weddell Sea. *Mon. Wea. Rev.*, **103**, 45–51.
- Spall, M. A., and J. F. Price, 1998: Mesoscale variability in Denmark Strait: The PV outflow hypothesis. *J. Phys. Oceanogr.*, **28**, 1598–1623.
- von Appen, W.-J., 2012: Moored observations of shelfbreak processes at the inflow to and outflow from the Arctic Ocean. Ph.D. thesis, Massachusetts Institute of Technology and Woods Hole Oceanographic Institution, Cambridge/Woods Hole, MA, 275 pp.
- Williams, W. J., E. C. Carmack, K. Shimada, H. Melling, K. Aagaard, R. W. Macdonald, and G. R. Ingram, 2006: Joint effects of wind and ice motion in forcing upwelling in Mackenzie Trough, Beaufort Sea. *Cont. Shelf Res.*, **26**, 2352–2366, doi:10.1016/j.csr.2006.06.012.